Hydrogen adatoms on graphene: The role of hybridization and lattice distortion

Keian Noori [1], Su Ying Quek [1,2] and Aleksandr Rodin [3,1]

[1]*Centre for Advanced 2D Materials, National University of Singapore, 6 Science Drive 2, 117546, Singapore*
[2]*Department of Physics, National University of Singapore, 2 Science Drive 3, 117542, Singapore*
[3]*Yale-NUS College, 16 College Avenue West, 138527, Singapore*

By performing a detailed study of hydrogen adsorbates on graphene using density functional theory (DFT), we propose a general tight-binding (TB) formalism for a simultaneous treatment of multiple impurities of arbitrary species. To elucidate the details of the hydrogen-graphene bonding, we systematically examine the effects of hybridization and deformation on the band structure and the spectral function. An enhanced understanding of the binding mechanisms leads to a TB model whose predicted spectral function compares favorably with the DFT calculations on the scale of the supercell, as well as the individual adsorbates and carbon atoms. The computational load of our model scales with the number of impurities, not their separation, making it especially useful for experimentally relevant clustered impurity configurations that are too computationally expensive for DFT. The formalism described here allows for the treatment of Anderson impurities and impurities that bind to multiple carbon atoms.

I. INTRODUCTION

Hydrogen is one of the most-studied graphene adsorbates. It has been shown, for example, that it can give rise to magnetism [1–4], enhance spin-orbit coupling [5,6], and lead to spin relaxation [7] and magnetoresistance [8]. Furthermore, the single-orbital hydrogen atom is the prototypical localized state in the problems of impurity-impurity interactions [9–11] and charge-density oscillations [12]. An accurate description of the interaction between hydrogen adatoms and the underlying graphene lattice is, therefore, crucial to studying these diverse phenomena.

While density functional theory (DFT) can describe the effects of hydrogen adsorption accurately, *ab initio* modeling of impurity clusters requires unfeasibly large computational cells. Moreover, even for dilute impurity concentrations, commonly used periodic boundary conditions cause undesirable interactions between adatoms in neighboring images (even for very large cells) [3,11], and can induce a spurious band gap in certain cases [13].

A suitable tight-binding (TB) model can, in principle, overcome these limitations. Earlier work has utilized two main approaches to describe hydrogen adatoms on graphene: coupling an impurity orbital to carbon atoms [12,14,15], or treating the host carbons as vacancies [3,8,16]. For the latter approach, the carbon-hydrogen bond has been described as the removal of a p_z orbital from graphene, creating a magnetic pseudovacancy [3,8,15,16], and the spectral function of the super cell with a single hydrogen adsorbate has been shown to be quite similar to the result for a single vacancy [14,15,17,18]. This missing-orbital model was successfully utilized in Ref. [8], where the authors used a TB mean-field Hubbard model and a supercell with hundreds of carbon atoms to calculate the system magnetization induced by the missing orbital.

Advances in experimental techniques have made it possible to study the effects that individual and clustered impurities have on the bulk charge density and magnetization in both graphene and other two-dimensional (2D) materials [3,19,20]. In Ref. [3], it was demonstrated that the magnetization can be switched on and off by changing the relative positions of hydrogen adatoms. Reference [19] shows complex interference patterns in spatially resolved dI/dV measurements, corresponding to the Friedel oscillations originating from multiple impurities. Finally, in Ref. [20] the authors use real-space Friedel oscillations produced by single hydrogen adsorbates and hydrogen dimers to study the Berry phase. Therefore, a model that can accurately handle multiple impurities simultaneously is highly desirable.

Although most theoretical work dealing with hydrogen impurities in graphene focuses on individual adsorbates, multiple adsorbates have been previously addressed in Ref. [12], where the authors employed the Born approximation to study substitutional defects and calculated the impurity-induced charge density in the form of Friedel oscillations. In the present work, we propose a nonperturbative approach to describe multiple impurities without any positional restrictions.

To elucidate the effects of hydrogen adsorption on graphene, we perform detailed DFT calculations and study the interplay between lattice deformation and hybridization. Our results reveal that the hydrogen-hosting carbon maintains interaction with its neighbors even after adsorption-induced lattice buckling. Therefore, we construct a multi-impurity TB model to include this effect. An additional benefit of explicitly treating the impurity as an orbital is the possibility of using the Anderson model [21] to study the impurity magnetization. While in this work we limit our comparison of TB and DFT results to hydrogen adsorbates, our formalism applies equally well to general adatom species with an arbitrary arrangement.
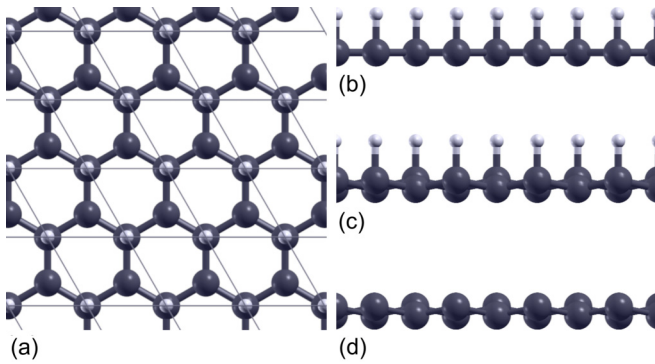
FIG. 1. (a) Semihydrogenated planar graphene. The borders of the unit cell are drawn as gray lines. The cross sections of (b) planar and (c) structurally relaxed SH graphene, as well as (d) buckled graphene are also shown.
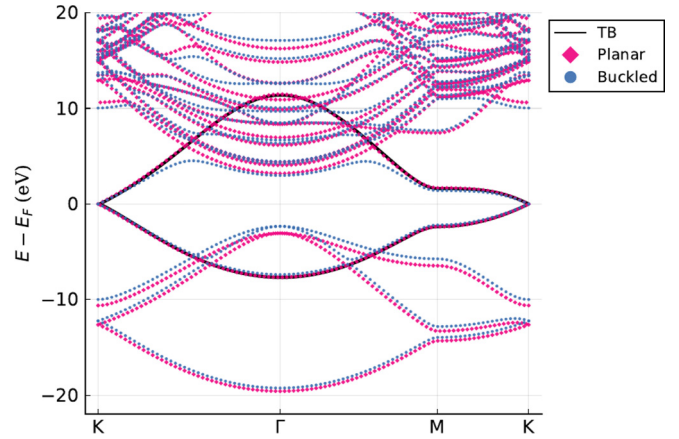

FIG. 2. *Ab initio* band structures for planar and buckled graphene. The solid black line is the seventeen-parameter tight-binding model from Ref. [22].

Using quantum field theory (QFT), we demonstrate how one can calculate the spectral function, local charge density, and the interaction energy for a general impurity configuration.

This paper is organized as follows. In Sec. II, we study the effects that extreme adsorption-induced lattice deformation has on the electronic properties of graphene. We observe that even a non-negligible $10°$ bucking does not substantially warp the relevant bands. We also examine the semihydrogenated (SH) graphene configuration, using DFT and TB, to understand the role that buckling plays in the adatom-graphene interaction. These observations allow us to create a simplified graphene-impurity TB model, introduced in Sec. III, which is used to explore individual hydrogen adatoms on graphene. A brief discussion on the effects of deformation on magnetization can be found in Sec. III C. We demonstrate our model's ability to handle multiple impurities of various types for different separations in Sec. IV. The computational methods are provided in Sec. V. Finally, Sec. VI contains the concluding remarks.

II. SEMIHYDROGENATED GRAPHENE

To illustrate the effects that hydrogen adatoms have on graphene, while isolating the role of the adsobate-induced buckling, we perform four band structure calculations: one for pristine graphene, two for SH graphene with and without structural relaxation, and one for buckled graphene. For the SH configurations, all the atoms of one of the graphene sublattices host a hydrogen adatom. The buckled graphene has the same lattice distortion as the relaxed SH monolayer, but without the hydrogen adatoms. The SH and buckled lattices are shown in Fig. 1.

In the buckled configuration, one of the sublattices is elevated above the original graphene plane. The angle between the original plane and the bond connecting the elevated atoms to their neighbors is about $10.3°$, or slightly more than half of the angle in a true sp^3 hybridization, where it is $19.5°$. Note that when we relax the SH lattice, graphene is not allowed to contract laterally in response to the out-of-plane deformation because we do not expect a substantial system-wide structural modification due to individual impurities, which are the main subjects of this study. Thus, in the relaxed SH and buckled

configurations, the bond length between neighboring carbon atoms becomes 1.44 Å and a vertical interatomic separation is 0.26 Å. For the sake of consistency, the hydrogen-carbon bond length for planar SH lattice is fixed to the value obtained for the relaxed SH lattice (1.18 Å).

Lattice buckling breaks the planar symmetry of the graphene monolayer and introduces coupling between previously isolated bands. The consequences of this interaction can be most clearly seen in Fig. 2, which shows the comparison between the planar and buckled graphene band structures. We observe a strong modification of the upper branch of the buckled graphene p_z band due to the mixing with the high-energy states. In addition, the new coupling creates an avoided crossing between π and σ valence bands at ≈ -7 eV, though the smallness of this level repulsion indicates that the deformation-induced interaction between p_z and the other carbon valence orbitals is fairly weak.

Comparison of the band structures also reveals that the lattice deformation does not substantially modify the shape of the low-energy bands. Instead, it changes the energy separation between the π and σ bands, introducing small, rigid energy shifts in these bands with respect to their planar counterparts. A closer look reveals that the buckled bands are marginally flatter compared to the planar ones (seen best for the lower branch of the π), which can be attributed to a very modest weakening of the carbon-carbon coupling due to the bond elongation. The robustness of the band structure shape means that the adsorption-induced lattice deformation is quite inconsequential for the coupling between the carbon valence orbitals.

In addition to the DFT band structures, we also plot a TB dispersion for the π bands in Fig. 2. This dispersion is calculated from the seventeen-parameter TB model for the p_z orbitals obtained from the maximally localized Wannier functions in Ref. [22]. The TB model gives an excellent agreement with the DFT result for the pristine monolayer, as can be seen in Fig. 2, where the solid TB curve follows the *ab initio* p_z-orbital bands. For the buckled system, the TB bands follow the DFT results very well up to the energies where the deformation-induced mixing with higher
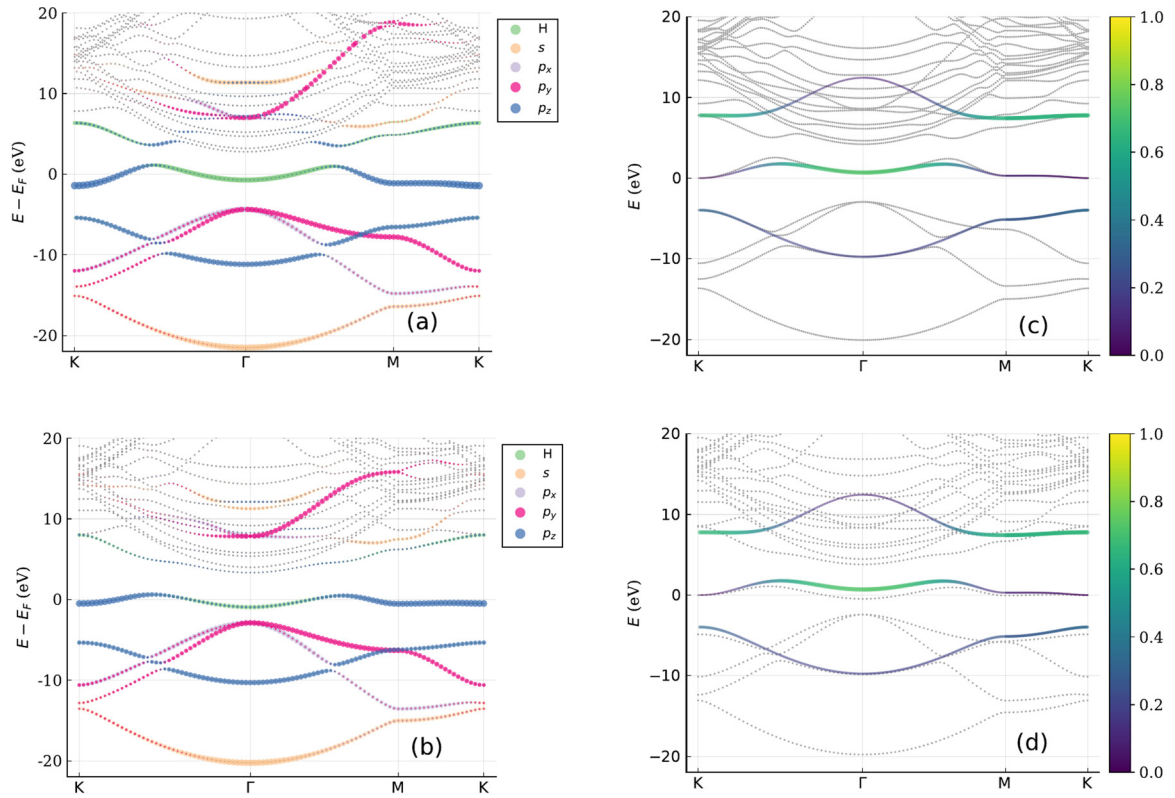
FIG. 3. DFT band structures SH planar (a) and relaxed (b) graphene. The thin gray lines are all the bands, while the colored overlays illustrate the contribution of individual hydrogen and carbon valence orbitals. The size of the colored markers corresponds to the amount of a given orbital in a particular state. (c) TB fit for the H_s/C_{p_z} bands for the flat SH lattice in panel (a) using Eq. (1). The color scale and the line thickness reflect the contribution of the hydrogen orbital to a given state. The upper TB band can be uncovered in (a) by following the trail of blue p_z orbitals along the higher-energy bands. (d) TB approximation for the relaxed lattice in panel (b). Here, the parameters ε, h, and V_0 are the same as in (c), while the rest are set to zero.

bands becomes important. Because the TB model describes the buckled monolayer well in the energy range of interest, we will use it in our description of graphene for the relaxed SH system.

Next, we consider a flat SH lattice. Our aim here is to construct a TB model that correctly captures the coupling between the adatoms and graphene using the pristine-graphene model from Ref. [22] as the starting point. The DFT band structure is given in Fig. 3(a), where we show the contributions of the carbon and hydrogen valence orbitals to the band composition. The hydrogen s orbital sits above the graphene plane and therefore can couple to all the carbon valence orbitals. Because of this interaction, both the π and σ graphene bands mix with the impurity and thus indirectly couple to each other. The effects of this mixing can be seen as the avoided band crossings in the valence bands at ≈ -9 eV.

Comparing the band structure of the flat SH system to that of pristine graphene, it is clear that the valence σ bands remain relatively unaltered by the addition of hydrogen. The apparent downward energy shift of the SH σ bands is a consequence of a raised Fermi level due to the electrons contributed by the hydrogen adatoms.

Unlike the σ bands, the graphene π bands undergo a substantial modification when the hydrogen atoms are added to the

system. From the band composition, it is obvious that, aside from the points of avoided crossing, the lower distorted π bands contain primarily carbon's p_z and hydrogen's s orbitals. Therefore, as we construct the TB model, we ignore the coupling of hydrogen to the non-p_z carbon orbitals.

In the absence of graphene, the hydrogen atoms form a triangular lattice with an interatomic distance of 2.46 Å and lattice vectors $\mathbf{d}_1$ and $\mathbf{d}_2$ identical to those of graphene. Because of the relatively large separation with respect to the size of a hydrogen atom, it is not unreasonable to assume that, from the TB perspective, the interaction strength between hydrogen atoms decreases sharply past the first nearest neighbors. Retaining only the nearest-neighbor interaction gives rise to a single energy band $E_{\mathbf{q}}^H = \varepsilon + h f_{2,\mathbf{q}}$, where ε is the on-site energy, h is the hopping term, and $f_{2,\mathbf{q}} = 2[\cos(\mathbf{d}_1 \cdot \mathbf{q}) + \cos(\mathbf{d}_2 \cdot \mathbf{q}) + \cos((\mathbf{d}_1 - \mathbf{d}_2) \cdot \mathbf{q})]$. Note that $f_{2,\mathbf{q}}$ is also the phase of the second nearest neighbor hopping in graphene. For $h < 0$, this hydrogen band has a minimum at Γ, a maximum at K, and a saddle point at M.

When graphene is introduced, hydrogen couples to its p_z orbitals and any degeneracy between the p_z and the hydrogen bands is lifted. In Fig. 3(a), this level repulsion takes the form of the avoided crossing at ≈ 3 eV between the green impurity band and the blue π branch.

To describe the interaction between the hydrogen lattice and graphene, we write the TB Hamiltonian as

$$H_{\mathbf{q}} = \begin{pmatrix} \varepsilon + h f_{2,\mathbf{q}} & V_0 + V_2 f_{2,\mathbf{q}} & V_1 f_{1,\mathbf{q}} + V_3 f_{3,\mathbf{q}} \\ V_0 + V_2 f_{2,\mathbf{q}} & H_{AA} & H_{AB} \\ V_1 f_{1,\mathbf{q}}^* + V_3 f_{3,\mathbf{q}}^* & H_{AB}^* & H_{BB} \end{pmatrix},$$
(1)

where V_j is the coupling to the jth nearest neighbor of a given hydrogen atom and $f_{j,\mathbf{q}}$ is the corresponding phase factor. The bottom-right 2×2 block is the seventeen-parameter graphene TB Hamiltonian. [22] Note that we modify the carbon on-site energy from Ref. [22] to ensure that the Dirac point is at $E = 0$.

There are several methods available to determine the six parameters in Eq. (1). One would be to perform a least-squares fitting of the bands computed from Eq. (1) to the relevant DFT bands over the entire BZ. The main weakness of this approach in the present context comes from the fact the the upper band of Eq. (1) lies in the range where the coupling with high-energy bands is substantial, except at certain high-symmetry points, making the fit unreliable. This can be understood from Fig. 3(a), where the top p_z is seen to mix strongly with other bands. Another approach, followed here, is to choose six energies λ_k at high-symmetry points composed of the relevant orbitals and, by enforcing $\det(H_{\mathbf{q}} - \lambda_k) = 0$, obtain ε, h, V_0, V_1, V_2, and V_3. The states that we pick are the highest- and lowest-energy H_s/C_{p_z} states at the K point and the two lowest H_s/C_{p_z} states at the Γ and M points. Using the lower band energies at the Γ and M points ensures that the fit is performed on the states with the correct composition. At the K point, the middle-energy state is composed entirely of the nonhost p_z orbital, while the other two states are made almost exclusively of the host p_z and the adsorbate orbital. The resultant parameter values are $\varepsilon \approx 2.44$ eV, $h \approx -0.457$ eV, $V_0 \approx -5.55$ eV, $V_1 \approx -0.245$ eV, $V_2 \approx 0.0026$ eV, and $V_3 \approx 0.0734$ eV.

The TB fit, plotted in Fig. 3(c), shows an excellent agreement with the DFT results for the lowest band and the low-energy portion of the middle band. At higher energies, mixing with the orbitals not considered in our model becomes important. Nevertheless, it is still possible to resolve the traces of the top band in the DFT results, Fig. 3(a), by following the states containing the p_z orbitals.

Finally, we address the relaxed SH system, whose band structure is shown in Fig. 3(b). The buckling increases the distance between the hydrogen atoms and their hosts' neighbors, leading to a reduced coupling between them. To illustrate the effects of this reduced coupling, we again turn to TB. Due to the increased distance, we set, as a first approximation, $V_{1,3} = 0$. For simplicity, we also neglect V_2 because of its smallness. The results of the TB calculations are shown in Fig. 3(d). This simplified model correctly captures the flatter dispersion of the middle band and is in a fairly good agreement with the lowest band, even though the fit was calculated for a system with a substantially different structure.

III. INDIVIDUAL ADATOMS

We begin this section by constructing an analytical model for a general arrangement of adatoms. We then demonstrate the quality of this model by comparing the spectral functions obtained from it to the projected density of states (PDOS) calculated using DFT for a single hydrogen adatom. We stress that while our analysis focuses on individual hydrogen adsorbates, the formalism presented below is general and can be used for arbitrary numbers of different impurity species. The method provided here is reminiscent of the approach in Refs. [4,15,23]. The main difference is that our formalism allows for the simultaneous treatment of multiple impurities of different types. Finally, we use DFT to show how buckling promotes the formation of magnetic states.

A. Analytical model

To describe an infinitely large graphene system hosting multiple impurity states simultaneously, we use the following Hamiltonian:

$$\hat{H} = \sum_{\mathbf{q}} c_{\mathbf{q}}^{\dagger} (H_{0,\mathbf{q}}^G - \mu) c_{\mathbf{q}} + \sum_k g_k^{\dagger} (\varepsilon_k - \mu) g_k$$

$$+ \sum_{jk} \left[c_{\mathbf{R}_j}^{\dagger} I_j V_{j,k} g_k + g_k^{\dagger} (V_{j,k})^* I_j^T c_{\mathbf{R}_j} \right]$$

$$+ \sum_{jl} c_{\mathbf{R}_j}^{\dagger} I_j \Delta_{jl} I_l^T c_{\mathbf{R}_l}.$$
(2)

Here, $H_{0,\mathbf{q}}^G$ is the pristine graphene Hamiltonian matrix, μ is the chemical potential, and $c_{\mathbf{q}}^{\dagger} = (a_{\mathbf{q}}^{\dagger} \quad b_{\mathbf{q}}^{\dagger})$ is a vector of the creation operators for the carbon p_z orbitals for the two sublattices in momentum space, while $c_{\mathbf{R}}^{\dagger}$ is its real-space counterpart. $g_k^{\dagger}$ is the creation operator for the impurity state of energy ε_k. The second line describes the coupling between the impurity states and graphene atoms at unit cells with coordinates $\mathbf{R}_j$. Importantly, the sum j runs over *all* the atoms impacted by the impurities, either by directly interacting with them or because the induced lattice deformation changes their coupling to other graphene atoms. To keep track of matrix dimensions, we denote the number of affected atoms by M and the number of impurity states by K. The quantity $I_j^T = (1 \quad 0)$ or $(0 \quad 1)$, depending on the sublattice of the atom j, and $V_{j,k}$ is atom j's interaction strength with the impurity state k. Finally, the last line gives the perturbation of the graphene Hamiltonian due to the lattice deformation. As with the line above, the sum includes all the modified atoms.

Before proceeding further, we highlight three important aspects of the model. First, what we refer to as the "impurity state" is not just the adatom orbital. Rather, as a consequence of hybridization, it also includes contributions from graphene orbitals not included in the model. As a consequence, the energy ε_k can depend on the carbon-adatom bond length, among other factors, as it influences the magnitude of the orbital interaction. Second, the impurity states are not orthogonal to the graphene Wannier functions due to a finite overlap integral. Equation (2) assumes that the overlap is small and neglects it by treating all the states in the system as orthogonal. While it is possible to extend the treatment to nonorthogonal states, this is outside the scope of our paper. Finally, even though the Hamiltonian in Eq. (2) includes only the carbon p_z orbitals, the subsequent derivation does not depend on this fact. Put differently, to include more orbitals in the model, one simply

needs to modify $H_{0,\mathbf{q}}^G$ and adjust the dimensions of I_j in the final result. In this case, the j and l summations run over *orbitals*, not *atoms*.

Using $c_{\mathbf{R}}^\dagger = N^{-1/2} \sum_{\mathbf{q}} c_{\mathbf{q}}^\dagger e^{-i\mathbf{R}\cdot\mathbf{q}}$, where N is the number of unit cells in the system, we write

$$\sum_j c_{\mathbf{R}_j}^\dagger I_j V_{j,k} = \frac{1}{\sqrt{N}} \sum_{\mathbf{q}} c_{\mathbf{q}}^\dagger \underbrace{\left(\sum_j e^{-i\mathbf{R}_j\cdot\mathbf{q}} I_j V_{j,k} \right)}_{\Theta_{\mathbf{q}}^\dagger \mathbf{I} V_{,k}}, \quad (3)$$

where $\Theta_{\mathbf{q}}$ is a column vector of $\mathbf{1}_{2\times2} e^{i\mathbf{R}_j\cdot\mathbf{q}}$ for all $\mathbf{R}_j$, $\mathbf{I}$ is a diagonal matrix of I_j, and $V_{,k}$ is a column vector of $V_{j,k}$. Similarly,

$$\sum_{jk} c_{\mathbf{R}_j}^\dagger I_j \Delta_{jk} I_k^T c_{\mathbf{R}_k} = \frac{1}{N} \sum_{\mathbf{qq'}} c_{\mathbf{q}}^\dagger \Theta_{\mathbf{q}}^\dagger \mathbf{I}\Delta\mathbf{I}^T \Theta_{\mathbf{q'}} c_{\mathbf{q'}}, \quad (4)$$

where Δ is an $M \times M$ matrix.

Plugging Eqs. (3) and (4) into Eq. (2), we transcribe the Hamiltonian into the imaginary time action

$$S = \sum_{\omega_n\mathbf{qq'}} \bar{\psi}_{\omega_n\mathbf{q}} \overbrace{\left[(-i\omega_n - \mu)\delta_{\mathbf{qq'}} + H_{\mathbf{qq'}}^G \right]}^{-G_{i\omega_n+\mu,\mathbf{qq'}}^{-1}} \psi_{\omega_n\mathbf{q'}}$$

$$+ \sum_{\omega_n k} \bar{\gamma}_{\omega_n,k} \overbrace{(-i\omega_n - \mu + \varepsilon_k)}^{-\Gamma_{0,i\omega_n+\mu,k}^{-1}} \gamma_{\omega_n,k}$$

$$+ \frac{1}{\sqrt{N}} \sum_{\omega_n k\mathbf{q}} (\bar{\psi}_{\omega_n,\mathbf{q}} \Theta_{\mathbf{q}}^\dagger \mathbf{I} V_{,k} \gamma_{\omega_n,k}$$

$$+ \bar{\gamma}_{\omega_n,k} V_{,k}^\dagger \mathbf{I}^T \Theta_{\mathbf{q}} \psi_{\omega_n,\mathbf{q}}). \quad (5)$$

Note that we have combined the $\mathbf{q}$-diagonal and non-diagonal portions of the graphene Hamiltonian into $H_{\mathbf{qq'}}^G$. The quantity ω_n is the fermionic Matsubara frequency, and γ and ψ are Grassmann fields. Integrating e^{-S} over all the fields yields the partition function

$$\mathcal{Z} = \prod_{\omega_n} \left| -\beta G_{i\omega_n+\mu}^{-1} \right| \left| -\beta \left(\Gamma_{0,i\omega_n+\mu}^{-1} - \frac{V^\dagger \mathbf{I}^T \Theta G_{i\omega_n+\mu} \Theta^\dagger \mathbf{I} V}{N} \right) \right|$$

$$= \prod_{\omega_n} \left| -\beta \Gamma_{0,i\omega_n+\mu}^{-1} \right| \left| -\beta \left(G_{i\omega_n+\mu}^{-1} - \frac{\Theta^\dagger \mathbf{I} V \Gamma_{0,i\omega_n+\mu} V^\dagger \mathbf{I}^T \Theta}{N} \right) \right|, \quad (6)$$

where Θ as a row vector of $\Theta_{\mathbf{q}}$ and V is an $M \times K$-dimensional matrix. Defining a pristine graphene Green's function $G_z^0 = (z - H_0^G)^{-1}$, we get

$$G_z = \left[(G_z^0)^{-1} - \frac{1}{N}\Theta^\dagger \mathbf{I}\Delta\mathbf{I}^T \Theta \right]^{-1}$$

$$= G_z^0 + \frac{1}{N} G_z^0 \Theta^\dagger \mathbf{I}\Delta(1 - \mathbf{I}^T \mathbf{\Xi}_z \mathbf{I}\Delta)^{-1} \mathbf{I}^T \Theta G_z^0, \quad (7)$$

where $\mathbf{\Xi}_z = \Theta G_z^0 \Theta^\dagger / N$ with entries $\mathbf{\Xi}_z^{jk} = \mathbf{\Xi}_z^{\mathbf{R}_j-\mathbf{R}_k}$ and

$$\mathbf{\Xi}_z^{\mathbf{R}} = \frac{1}{N} \sum_{\mathbf{q}} G_{z\mathbf{q}}^0 e^{i\mathbf{R}\cdot\mathbf{q}}. \quad (8)$$

G_z is the graphene Green's function including the lattice deformation, but not the effects of the impurity states.

In the parentheses of the first line of Eq. (6), we identify the inverse of the full impurity Green's function, denoted by Γ_z^{-1}:

$$\Gamma_z = \left(\Gamma_{0,z}^{-1} - V^\dagger \Lambda_z V \right)^{-1}$$

$$= \Gamma_{0,z} + \Gamma_{0,z} V^\dagger \Lambda_z (1 - V \Gamma_{0,z} V^T \Lambda_z)^{-1} V \Gamma_{0,z}, \quad (9)$$

$$\Lambda_z = \mathbf{I}^T \mathbf{\Xi}_z \mathbf{I}[1 + \Delta(1 - \mathbf{I}^T \mathbf{\Xi}_z \mathbf{I}\Delta)^{-1} \mathbf{I}^T \mathbf{\Xi}_z \mathbf{I}]. \quad (10)$$

Also, from the parentheses of the second line in Eq. (6), we obtain the inverse of the full graphene Green's function, given by

$$\mathcal{G}_z = \left[(G_z^0)^{-1} - \frac{1}{N}\Theta^\dagger \mathbf{I}(\Delta + V\Gamma_{0,z}V^\dagger)\mathbf{I}^T \Theta \right]^{-1}$$

$$= G_z^0 + \frac{1}{N} G_z^0 \Theta^\dagger \mathbf{I}D_z \mathbf{I}^T \Theta G_z^0, \quad (11)$$

$$D_z = [(\Delta + V\Gamma_{0,z}V^\dagger)^{-1} - \mathbf{I}^T \mathbf{\Xi}_z \mathbf{I}]^{-1}. \quad (12)$$

Using Eq. (11), it is possible to calculate the real-space graphene Green's function $\mathcal{G}_{i\omega_n+\mu,\mathbf{R}}^s = N^{-1} \sum_{\mathbf{qq'}} \langle \bar{\psi}_{\omega_n\mathbf{q}}^s \psi_{\omega_n\mathbf{q'}}^s \rangle e^{i(\mathbf{q'}-\mathbf{q})\cdot\mathbf{R}}$, where s denotes the sublattice and the correlation functions are the diagonal elements of the $[\mathcal{G}_{i\omega_n+\mu}]_{\mathbf{q'q}}$ blocks:

$$\mathcal{G}_{z,\mathbf{R}} = \mathbf{\Xi}_z^{\mathbf{0}} + \sum_{jk} \mathbf{\Xi}_z^{\mathbf{R}-\mathbf{R}_j} (\mathbf{I}D_z\mathbf{I}^T)_{jk} \mathbf{\Xi}_z^{\mathbf{R}_k-\mathbf{R}}$$

$$= \mathbf{\Xi}_z^{\mathbf{0}} + (\mathbf{\Xi}_z^{\mathbf{R}-\mathbf{R}_1} \quad \cdots)\mathbf{I}D_z\mathbf{I}^T \begin{pmatrix} \mathbf{\Xi}_z^{\mathbf{R}_1-\mathbf{R}} \\ \vdots \end{pmatrix}. \quad (13)$$

By taking the kth diagonal entry of $-2\,\text{Im}\,[\Gamma_{\omega+i0^+}]$ and $-2\,\text{Im}\,[\mathcal{G}_{\omega+i0^+,\mathbf{R}}^s]$, we obtain the spectral functions for the kth impurity and the corresponding carbon atom, respectively. These spectral functions can be compared directly to the DFT-computed PDOS. By integrating the Green's functions along the complex axis, we can obtain the occupation number of a graphene orbital or the impurity state. Finally, using the fact that the Helmholtz free energy $F = -T \ln \mathcal{Z}$, one can obtain the impurity interaction energy.

B. Spectral function and PDOS

To model individual hydrogen atoms using DFT, we increase the size of the graphene supercell hosting a single impurity to 10×10 unit cells. As before, we perform calculations using both planar and relaxed graphene while setting the carbon-hydrogen bond length to the value obtained for the relaxed configuration (1.13 Å). For the relaxed lattice, the bond length between the host carbon and its nearest neighbors is 1.50 Å with a vertical distance of 0.35 Å. The first neighbors, on the other hand, sit about 0.15 Å above the original plane (close to 0.08 Å above the second neighbors). As one goes farther from the impurity, the height difference between neighbors continues to decrease. We saw in the case of SH graphene that the vertical displacement of 0.25 Å does not drastically impact the band structure. In the present case, since, except for the host atom, all neighbors have a relative
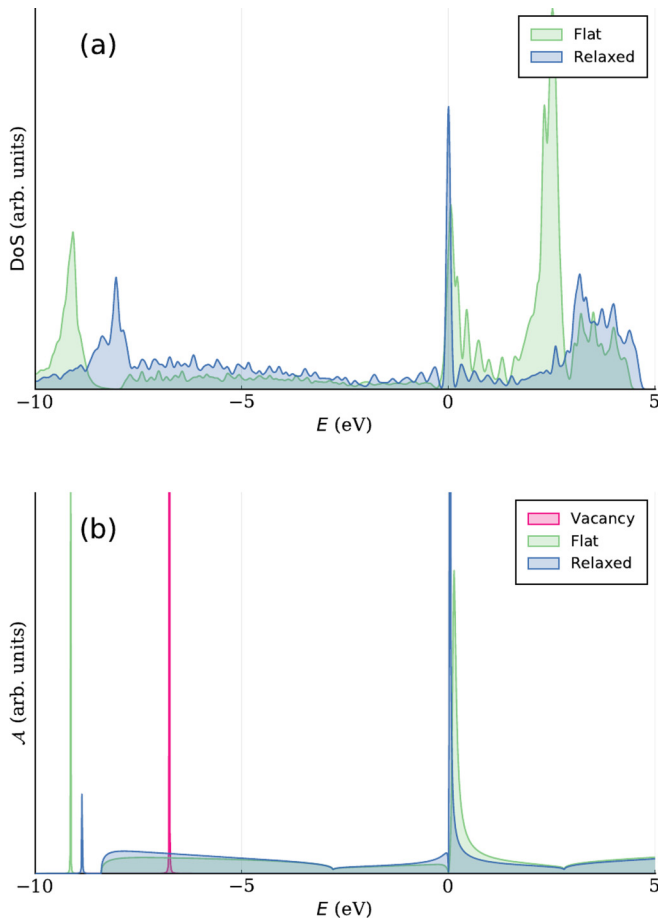
FIG. 4. (a) PDOS of the hydrogen s orbital for a 10×10 unit cell. (b) Spectral function of the impurity state.

vertical displacement that is substantially less than the SH value, it is reasonable to treat the rest of the lattice as flat.

The PDOS for the hydrogen s orbital is given in Fig. 4(a). While qualitatively similar, the flat and the relaxed results exhibit some differences. First, the peak around $E = 0$ is substantially broader for the flat configuration. This feature will become important when we discuss the system magnetization. Second, the broad low-energy peak for the flat PDOS is below the relaxed PDOS one.

For the spectral function, we need to calculate $\Xi_z^{\mathbf{R}}$ in Eq. (8), which requires $H_{0,\mathbf{q}}^G$. In the discussion above, we used a seventeen-parameter tight-binding Hamiltonian. While it is also possible to do so here, the necessary two-dimensional integrals significantly increase the numerical cost without substantially changing the qualitative picture. Therefore, we use the nearest-neighbor hopping Hamiltonian as it allows us to take one of the momentum integrals analytically. The loss of accuracy is not a major concern here since we expect inaccuracies in the results for high-energy states even for the more elaborate model because of the mixing with other bands. Furthermore, the minimal nearest-neighbor model used here captures the qualitative behavior of the low-energy states reasonably well. We refer the reader to the Appendix for the calculation of $\Xi_z^{\mathbf{R}}$.

To make use of Eqs. (9) and (13), we assume that the hydrogen adatom can interact with four carbon atoms (the host and its nearest neighbors) and that the hopping in graphene is modified only between the host and its neighbors. The motivation behind this assumption is to produce the minimal model that exhibits the principal features. The treatment is easily extendable to include more neighbors if greater numerical accuracy is desired. We use the information obtained in the previous section to make reasonable choices for the single-impurity TB parameters. For the hydrogen-carbon coupling, we take into account the reduced carbon-hydrogen bond length, as compared to the SH system, and use $V_0 = -7$ eV. To highlight the difference between the flat and the relaxed lattices, we set $V_1 = -0.2$ eV for the flat configuration and $V_1 = 0$ for the relaxed one, similar to the quantities we used for the SH graphene systems. We also reduce the hopping energy between the host and its neighbors by 5% for the relaxed system. Finally, we set $\varepsilon = 0.5$ eV. This value is smaller than what we obtained in the SH case and is guided by the position of the PDOS peak. We stress that the qualitative behavior of the spectral function is quite insensitive to the exact parameter choice.

The spectral function for the impurity, shown in Fig. 4(b), agrees well with the impurity PDOS in the energy range where the mixing with higher-energy bands can be neglected. Below the π-band range, the spectral function contains a pole corresponding to a localized state. If σ bands are included, this localized state mixes with them and broadens the peak, which is precisely what we observe in the PDOS.

It is important to note the spectral function peak at the Dirac point carries less than 10% of the impurity state's spectral weight. The fact that most of the impurity spectral weight is distributed over the bandwidth of the p_z graphene band is inconsistent with the vacancy picture. We also include the "vacancy" spectral function for the hydrogen atom, calculated by setting the coupling between the host carbon and its neighbors to zero.

We additionally calculate the PDOS and spectral function for the host carbon, as well as its first, second, and third nearest neighbors. The results are shown in Fig. 5, where it is clear that the salient DFT PDOS features are preserved across all corresponding spectral function panels. To improve the quantitative agreement between the two types of calculations, one can use a more complete TB model for the spectral function. This would bring the van Hove singularities closer to the Dirac point and produce a particle-hole asymmetry, as observed in the DFT PDOS of panels (c) and (e). Another source of differences between PDOS and the spectral function is the presence of additional bands in the DFT calculations, giving rise to extra features at low and high energies. A more complete Hamiltonian with additional orbitals and more hydrogen-carbon coupling terms is expected to produce a better agreement, especially if the nonorthogonality of the impurity state with respect to the graphene orbitals is taken into account.

The vacancy model is included in the TB plots of the spectral function. As expected, the greatest difference between the vacancy model and the adsorbate approach can be observed for the host carbon. As one moves farther away from the adsorption sites, the vacancy and adsorbate spectral functions
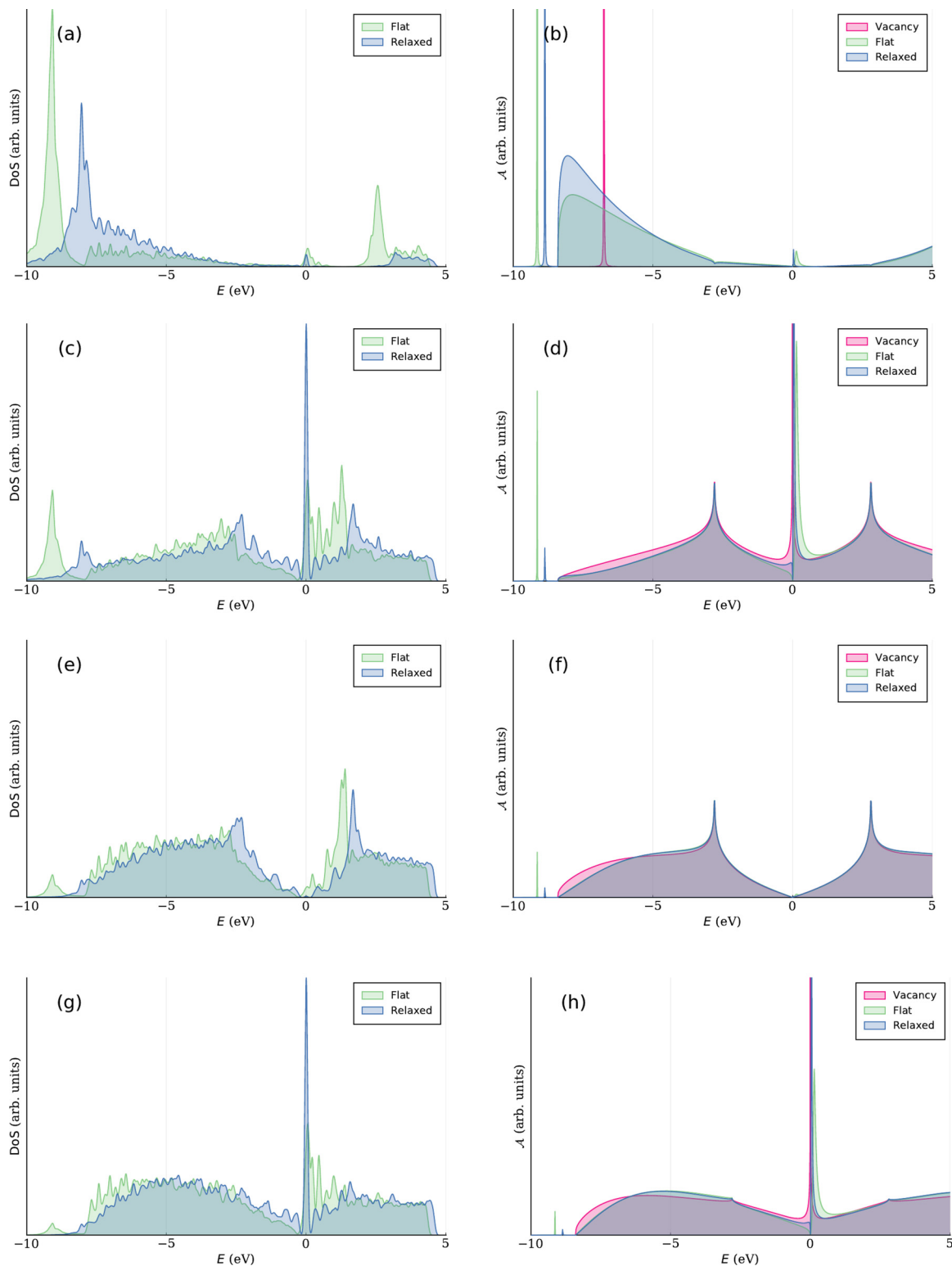
FIG. 5. PDOS (left column) and the spectral function (right column) for the p_z orbital of the host carbon (top row), and of the first, second, and third nearest neighbors (second, third, and fourth rows).

become progressively more similar, explaining why the super-cell PDOS for the vacancy looks so much like the PDOS for a supercell with a single hydrogen adsorbate [14,15,17,18]: the supercell PDOS is dominated by a large number of more distant neighbors. By comparing the PDOS to the spectral function for individual carbon orbitals, however, one can see

that the adsorbate approach replicates the DFT features more faithfully, even capturing the (broadened) poles below the bottom band edge.

Beyond giving a better agreement with the DFT results for distant neighbors, the adsorbate model provides the freedom to include more impurity effects. For example, one can treat
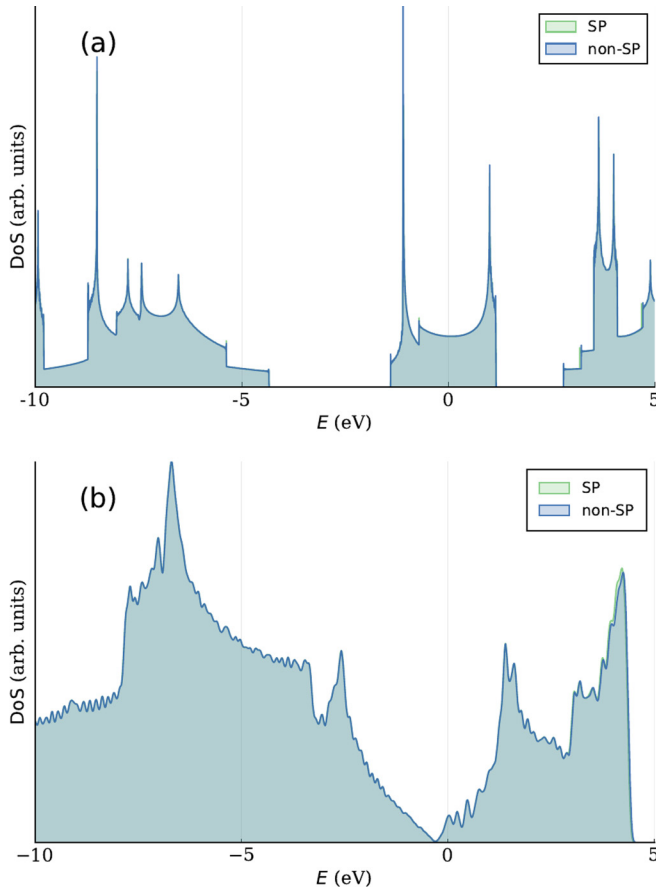
FIG. 6. Density of states of the planar SH cell (a) and 10×10 supercell (b) for spin-polarized and non-spin-polarized calculations.

FIG. 7. Density of states of the relaxed SH cell (a) and 10×10 supercell (b) for spin-polarized and non-spin-polarized calculations. The inset shows the region around the Dirac point of graphene.

the adsorbate as an Anderson impurity or allow it to couple to multiple carbon atoms simultaneously, both of which are impossible in the vacancy approach.

C. Buckling and spin polarization

The lattice deformation is important when one considers spin effects. It is known [5] that, in the presence of spin-orbit coupling, the mixing of graphene σ and π bands leads to spin-flip processes. Additionally, as we show below, the lattice deformation and the corresponding weakening of the adatom's coupling to more distant carbon atoms facilitate the formation of impurity-induced magnetization.

All *ab initio* electronic structure calculations so far were performed without spin polarization (i.e., the explicit inclusion of both spin up and down electrons in the description of the electronic density). Figure 6 shows the DOS of the planar SH cell and 10×10 supercell, both with and without spin polarization, from which we can see that the impact of spin polarization is minimal on the total DOS.

The situation is quite different for the relaxed lattice (Fig. 7), where the spin-polarized DOS of SH graphene and the 10×10 supercell demonstrate a clear peak splitting near the Fermi level which is absent in the non-spin-polarized cases and which leads to a finite magnetic moment. The peak splitting in the supercell is quite small [3] and is seen more clearly in the inset of Fig. 7(b).
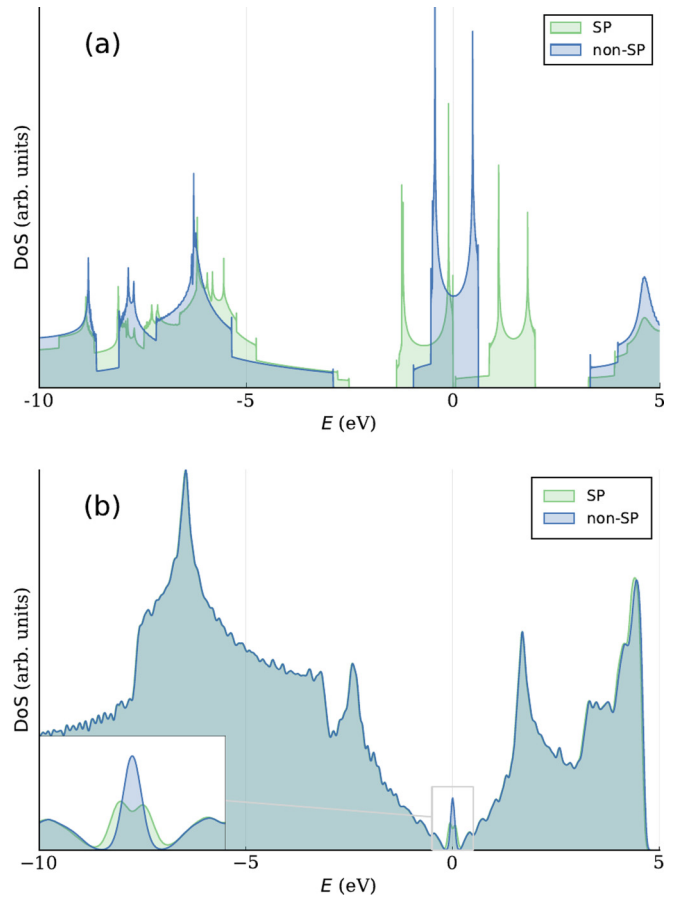
To understand how graphene buckling leads to magnetization, we turn again to Fig. 4. The reduced coupling between the impurity and its more distant neighbors in a buckled system, as compared to the flat one, produces a narrower spectral peak at the Dirac point. Let us now treat the impurity following Anderson's prescription [21], i.e., as a localized state with an on-site repulsion. It is known [21,24,25] that, for a fixed repulsion U, increasing the coupling between an Anderson impurity and the bulk suppresses the magnetization by reducing the window of the chemical potential where the system becomes magnetic. This relationship between increased coupling and reduced magnetization is consistent with our results, supporting the validity of treating the adsorbate as an Anderson impurity.

IV. LOCAL ELECTRON DENSITY

In addition to calculating spectral functions, our approach is well-suited for calculating the local impurity-induced electronic density, obtained by integrating the second term of Eq. (13) with $z \rightarrow i\omega + \mu$ for $-\infty < \omega < \infty$. To demonstrate the utility of our formalism, we plot the electronic density induced by six impurity states in Fig. 8. We reiterate that these results are obtained by treating all the impurities simultaneously in a nonperturbative fashion. The distance between
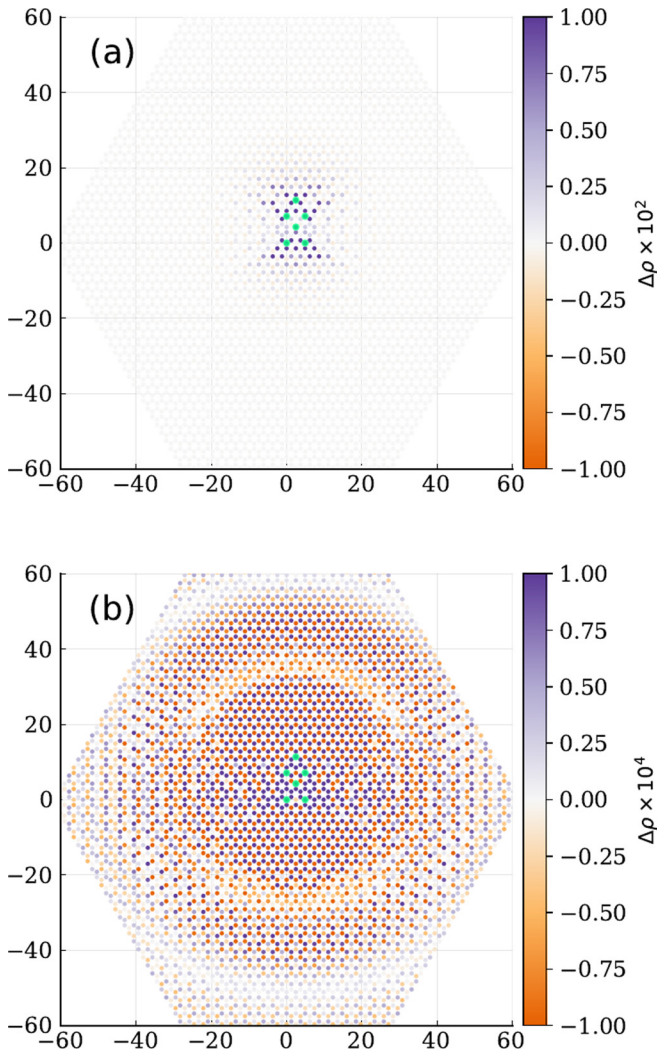
FIG. 8. Impurity-induced electronic density due to six impurities (light green dots). Here, the TB parameters are the same ones used for the buckled adsorbates and the chemical potential $\mu = 0.4$ eV. The difference between the two panels is the scale of $\Delta\rho$ given in electrons per atom. The x and y axes labels are in angstroms. The lower panel clearly illustrates the Friedel oscillations.
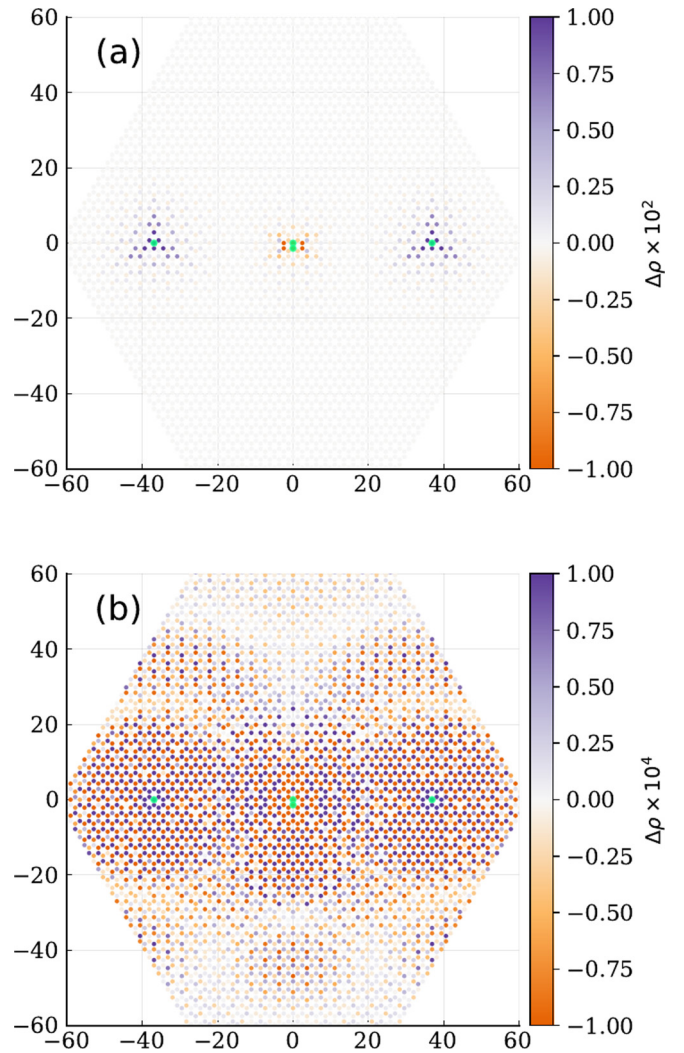
FIG. 9. Impurity-induced electronic density due to three impurities for $\mu = 0.4$ eV. Two of them (on the left and on the right) attach to a single carbon host, just like the adatoms in Fig. 8. The impurity in the middle couples to two neighboring carbon atoms from opposite sublattices.

the two most-separated impurities is 1.5 nm. In contrast to DFT calculations, which would be infeasible such an impurity configuration, our formalism is able to efficiently deal with this system since the computational load does not change with the impurity separation.

By plotting the charge density using two different scales, we demonstrate nontrivial charge modulation close to the impurities give way to Friedel oscillations farther away. Note that the charge density in the two sublattices do not have the same phase, as expected. [11,12]

We also show how our approach handles impurities of different types in Fig. 9. In addition to having two single-site impurities on the left and on the right of the region of interest, we position a single impurity in the middle, allowing it to couple to two neighboring carbon atoms. Fig. 9(b) demonstrates a nontrivial interference pattern as the Friedel oscillations

originating from the hydrogen-like absorbates become mixed by the central impurity.

V. METHODS

DFT calculations were performed with QUANTUM ESPRESSO [26,27] using a projector augmented wave (PAW) [28,29] basis and the Perdew-Burke-Ernzerhof (PBE) [30] exchange correlation functional. The kinetic energy cutoff of wave functions was set to 60 Ry. Structural relaxations were performed until the forces on all atoms were below 10 meV/Å and the energy difference between subsequent relaxation steps was below 0.0001 Ry. For band structure calculations, the charge densities of the systems were computed by sampling the Brillouin zones via unit-cell-equivalent uniform meshes of 36×36 k points. DOS calculations were performed using the tetrahedron method [31], with unit-cell-equivalent Brillouin zone samplings of 60×60 k points (charge density) and 120×120 k points (eigenvalues). A small Gaussian

broadening (~ 0.03 eV) was added to the eigenvalues of all DFT DOS plots. Numerical calculations of the model were performed using the JULIA programming language [32].

VI. CONCLUSIONS

Using hydrogen atoms as model adsorbates, we have performed a systematic study of the role played by lattice deformation and orbital hybridization to propose a TB formalism for dealing with multiple impurities in graphene simultaneously. The TB results show an excellent agreement with DFT calculations in the region of the model's validity. By treating the impurity orbital as a state coupled to graphene, we are able to obtain spectral functions for the impurity and the host atom that reproduce the most important features of the DFT-calculated PDOS. Specifically, the spectral weights of the host p_z orbital and the impurity s orbital become distributed over the entire bandwidth of the graphene π bands. This allows the magnetism produced by the Anderson mechanism to propagate through the bulk, resulting in nonzero local spin polarization. The numerical accuracy of the model can be improved in a straightforward manner by adding more neighbor couplings to the TB portion. Our nonperturbative approach is computationally efficient, scaling only with the number of impurities, and is able to handle arbitrary arrangements of adatoms of various species. This makes our model especially relevant for studying experimental scenarios where impurities are too close to each other to be regarded as independent, yet far enough to make DFT supercells unfeasibly large.

The DFT data and the code for the numerical calculations can be found at [33].

ACKNOWLEDGMENTS

APPENDIX: GRAPHENE PROPAGATOR

To compute $\Xi_z^{\mathbf{R}}$, we first introduce

$$\Omega_z^{u,v} = \frac{1}{N} \sum_{\mathbf{q} \in \mathrm{BZ}} \frac{e^{i\mathbf{q} \cdot (u\mathbf{d}_1 + v\mathbf{d}_2)}}{z^2 - t^2 |f_{1,\mathbf{q}}|^2} \tag{A1}$$

with $u\mathbf{d}_1 + v\mathbf{d}_2 = \frac{d}{2}(u - v, \sqrt{3}(u + v))$ and $t = 2.8$ eV as the nearest-neighbor hopping energy. Using $\mathbf{q} \cdot (u\mathbf{d}_1 + v\mathbf{d}_2) = \frac{d}{2}[(u - v)q_x + \sqrt{3}(u + v)q_y]$ and turning the momentum sum into an integral yields

$$\Omega^{u,v}(z) = \frac{1}{(2\pi)^2} \oint dx \oint dy$$
$$\times \frac{e^{i[(u-v)x+(u+v)y]}}{z^2 - t^2(1 + 4\cos^2 x + 4\cos x \cos y)}. \tag{A2}$$

From

$$\oint d\theta \frac{e^{il\theta}}{w - \cos\theta} = 2\pi \frac{\left(w - \sqrt{w-1}\sqrt{w+1}\right)^{|l|}}{\sqrt{w-1}\sqrt{w+1}}, \tag{A3}$$

we get

$$\Omega_z^{u,v} = \frac{1}{2\pi} \frac{1}{4t^2} \oint dx \frac{e^{i(u-v)x}}{\cos x} \frac{\left(W - \sqrt{W-1}\sqrt{W+1}\right)^{|u+v|}}{\sqrt{W-1}\sqrt{W+1}}, \tag{A4}$$

$$W = \frac{\frac{z^2}{t^2} - 1}{4\cos x} - \cos x. \tag{A5}$$

Finally, $\Xi_z^{\mathbf{R}}$ for $\mathbf{R} = u\mathbf{d}_1 + v\mathbf{d}_2$ can be written as

$$\Xi_z^{\mathbf{R}} = \begin{pmatrix} z\Omega_z^{u,v} & -t\left[\Omega_z^{u,v} + \Omega_{+,z}^{u,v}\right] \\ -t\left[\Omega_z^{u,v} + \Omega_{-,z}^{u,v}\right] & z\Omega_z^{u,v} \end{pmatrix}, \tag{A6}$$

$$\Omega_{\pm,z}^{u,v} = \frac{1}{2\pi} \frac{1}{4t^2} \oint dx$$
$$\times 2e^{i(u-v)x} \frac{\left(W - \sqrt{W-1}\sqrt{W+1}\right)^{|u+v\pm 1|}}{\sqrt{W-1}\sqrt{W+1}}. \tag{A7}$$

[1] O. V. Yazyev and L. Helm, Phys. Rev. B **75**, 125408 (2007).

[2] D. W. Boukhvalov, M. I. Katsnelson, and A. I. Lichtenstein, Phys. Rev. B **77**, 035427 (2008).

[3] H. González-Herrero, J. M. Gómez-Rodríguez, P. Mallet, M. Moaied, J. J. Palacios, C. Salgado, M. M. Ugeda, J. Y. Veuillen, F. Yndurain, and I. Brihuega, Science **352**, 437 (2016).

[4] N. A. García-Martínez, J. L. Lado, D. Jacob, and J. Fernández-Rossier, Phys. Rev. B **96**, 024403 (2017).

[5] A. H. Castro Neto and F. Guinea, Phys. Rev. Lett. **103**, 026804 (2009).

[6] M. Gmitra, D. Kochan, and J. Fabian, Phys. Rev. Lett. **110**, 246602 (2013).

[7] M. R. Thomsen, M. M. Ervasti, A. Harju, and T. G. Pedersen, Phys. Rev. B **92**, 195408 (2015).

[8] D. Soriano, N. Leconte, P. Ordejón, J. C. Charlier, J. J. Palacios, and S. Roche, Phys. Rev. Lett. **107**, 016602 (2011).

[9] A. V. Shytov, D. A. Abanin, and L. S. Levitov, Phys. Rev. Lett. **103**, 016806 (2009).

[10] M. Agarwal and E. G. Mishchenko, Phys. Rev. B **99**, 085439 (2019).

[11] K. Noori, H. Biswas, S. Y. Quek, and A. Rodin, Phys. Rev. B **101**, 115421 (2020).

[12] J. A. Lawlor, S. R. Power, and M. S. Ferreira, Phys. Rev. B **88**, 205416 (2013).

[13] J. M. García-Lastra, Phys. Rev. B **82**, 235418 (2010).

[14] T. O. Wehling, S. Yuan, A. I. Lichtenstein, A. K. Geim, and M. I. Katsnelson, Phys. Rev. Lett. **105**, 056802 (2010).

[15] S. Irmer, D. Kochan, J. Lee, and J. Fabian, Phys. Rev. B **97**, 075417 (2018).

[16] D. Soriano, D. Van Tuan, S. M. Dubois, M. Gmitra, A. W. Cummings, D. Kochan, F. Ortmann, J. C. Charlier, J. Fabian, and S. Roche, 2D Mater. **2**, 022002 (2015).

[17] N. M. R. Peres, F. Guinea, and A. H. Castro Neto, Phys. Rev. B **73**, 125411 (2006).

[18] V. M. Pereira, J. M. B. Lopes dos Santos, and A. H. Castro Neto, Phys. Rev. B **77**, 115109 (2008).

[19] L. Chen, P. Cheng, and K. Wu, J. Phys.: Condens. Matter **29**, 103001 (2017).

[20] C. Dutreix, H. González-Herrero, I. Brihuega, M. I. Katsnelson, C. Chapelier, and V. T. Renard, Nature (London) **574**, 219 (2019).

[21] P. W. Anderson, Phys. Rev. **124**, 41 (1961).

[22] J. Jung and A. H. Macdonald, Phys. Rev. B **87**, 195450 (2013).

[23] N. A. Pike and D. Stroud, Phys. Rev. B **89**, 115428 (2014).

[24] B. Uchoa, V. N. Kotov, N. M. Peres, and A. H. Castro Neto, Phys. Rev. Lett. **101**, 026805 (2008).

[25] A. S. Rodin and A. H. Castro Neto, Phys. Rev. B **97**, 235428 (2018).

[26] P. Giannozzi, S. Baroni, N. Bonini, M. Calandra, R. Car, C. Cavazzoni, D. Ceresoli, G. L. Chiarotti, M. Cococcioni, I. Dabo, A. Dal Corso, S. De Gironcoli, S. Fabris, G. Fratesi, R. Gebauer, U. Gerstmann, C. Gougoussis, A. Kokalj, M. Lazzeri, L. Martin-Samos, N. Marzari *et al.*, J. Phys.: Condens. Matter **21**, 395502 (2009).

[27] P. Giannozzi, O. Andreussi, T. Brumme, O. Bunau, M. Buongiorno Nardelli, M. Calandra, R. Car, C. Cavazzoni, D. Ceresoli, M. Cococcioni, N. Colonna, I. Carnimeo, A. Dal Corso, S. De Gironcoli, P. Delugas, R. A. Distasio, A. Ferretti, A. Floris, G. Fratesi, G. Fugallo *et al.*, J. Phys.: Condens. Matter **29**, 465901 (2017).

[28] P. E. Blöchl, Phys. Rev. B **50**, 17953 (1994).

[29] A. Dal Corso, Comput. Mater. Sci. **95**, 337 (2014).

[30] J. P. Perdew, K. Burke, and M. Ernzerhof, Phys. Rev. Lett. **77**, 3865 (1996).

[31] P. E. Blöchl, O. Jepsen, and O. K. Andersen, Phys. Rev. B **49**, 16223 (1994).

[32] J. Bezanson, A. Edelman, S. Karpinski, and V. B. Shah, SIAM Rev. **59**, 65 (2017).

[33] https://github.com/rodin-physics/graphene-hydrogen.